**Light-Emitting Diodes** 



# Quantitative Multi-Scale, Multi-Physics Quantum Transport Modeling of GaN-Based Light Emitting Diodes

Junzhe Geng,\* Prasad Sarangapani, Kuang-Chung Wang, Erik Nelson, Ben Browne, Carl Wordelman, James Charles, Yuanchen Chu, Tillmann Kubis, and Gerhard Klimeck

The performance of nitride-based light emitting diodes is determined by carrier transport through multi-quantum-well structures. These structures divide the device into spatial regions of high carrier density, such as n-GaN/p-GaN contacts and InGaN quantum wells, separated by barriers with low carrier density. Wells and barriers are coupled to each other via tunneling and thermionic emission. Understanding of the quantum mechanics-dominated carrier flow is critical to the design and optimization of light-emitting diodes (LEDs). In this work a multi-scale quantum transport model, which treats high densities regions as local charge reservoirs, where each reservoir serves as carrier injector/receptor to the next/previous reservoir is presented. Each region is coupled to its neighbors through coherent quantum transport. The nonequilibrium Green's function (NEGF) formalism is used to compute the dynamics (states) and the kinetics (filling of states) of the entire device. Electrons are represented in multi-band tight-binding Hamiltonians. The I-V characteristics produced from this model agree quantitatively with experimental data. Carrier temperatures are found to be about 60 K above room temperature and the quantum well closest to the p-side emits the most light, in agreement with experiments. Auger recombination is identified to be a much more significant contributor to the LED efficiency droop than carrier leakage.

### 1. Introduction

GaN/InGaN multi-quantum-well (MQW) structures are the core technology of most mid-to-high power blue light-emitting diodes (LED). Light emission efficiency, or quantum efficiency at high drive current is critical to the performance of the LED. Key challenges in LED design include efficiency droop<sup>[1,2]</sup> and non-uniform light emission<sup>[3]</sup> among quantum wells. The active

Dr. J. Geng, P. Sarangapani, K.-C. Wang, J. Charles, Y. Chu, Prof. T. Kubis, Prof. G. Klimeck Network for Computational Nanotechnology Purdue University West Lafayette, IN 47907, USA E-mail: jgeng@purdue.edu Dr. E. Nelson, Dr. B. Browne, Dr. C. Wordelman

Lumileds,

370 W. Trimble Road, San Jose, CA 95131, USA

The ORCID identification number(s) for the author(s) of this article can be found under https://doi.org/10.1002/pssa.201700662.

DOI: 10.1002/pssa.201700662

region of a typical LED consists of multiquantum wells (MQW) that contain confined quantum states serving as recombination centers, and highly-doped n/p contacts providing electrons and holes from opposite ends into the MQW. The quantum wells (QWs), typically a few nanometer thick, are coupled to each other through tunneling and thermionic transport. These transport mechanisms as well as carrier capture into the QWs are integral part of the LED operation and need to be well understood. Carrier transport defined in a quantum system is therefore at the heart of the LED operation.

State-of-the-art modeling approaches for carrier transport in LEDs are based on drift-diffusion semiclassical models, which either heuristically patch in quantum effects<sup>[4]</sup> or simply ignore them. Shortcomings of such rather inconsistent carrier transport models often manifest in the prediction of unrealistic turn-on voltages. The Non-Equilibrium Green Function (NEGF) formalism is the accepted state-of-the-art carrier transport theory for a wide range of nanoscale semiconductor devices.<sup>[5–7]</sup> Under the NEGF formalism, tunneling, thermionic emission,<sup>[8]</sup> scatter-

ing<sup>[9]</sup> and recombination<sup>[10]</sup> are all treated on the same footing throughout the device. However, quantum mechanical treatment of all mechanisms, especially incoherent scattering, in a realistic LED has proven to be far too computationally expensive. Moreover, there is no accepted NEGF physics-based self-energy that leads to full thermalization in high carrier density device regions. Due to these challenges, NEGF modeling of LEDs have mostly been limited to proof-of-concept, applied on simplified device and/or with simplified band models.<sup>[10,11]</sup> Multi-scale approaches combining drift-diffusion and NEGF have been proposed recently,<sup>[12]</sup> however in such approaches, transport is based on semiclassical physics with NEGF correction and appropriate relaxation of carriers in the leads and QWs is not included.

In this work, a numerically efficient, multi-scale multi-physics NEGF model has been developed and applied to modeling a commercial LED device, and quantitatively reproduces its experimental I–V characteristics. Some preliminary results of this work have previously been published in Refs. <sup>[13,14]</sup>.

www.pss-a.com

# 2. Methodology

The main aspect of this methodology is to divide the LED device structure into sub-domains based on carrier scattering vs tunneling physics. **Figure 1** shows the band diagram of a typical AlInGaN LED active region. The LED structure contains an n-doped GaN layer, MQW consisting of barriers/wells made of  $GaN/In_xGa_{1-x}N$ ,  $Al_xGa_{1-x}N$  electron-blocking-layer (EBL) and a p-doped GaN layer. The Hamiltonian of the total device  $H_{Device}$  is divided as

$$H_{\text{Device}} = H_{LL} + H_{B1} + H_{W1} + \dots + H_{W6} + H_{B7} + H_{RL}$$
 (1)

here, LL and RL refer to the n-GaN and EBL plus p-GaN regions, respectively. Barriers (wells) are indicated with 'B' (W) followed by the corresponding numerical label shown in Figure 1. The device Hamiltonian is represented with atomistic tight-binding with 20 orbitals per atom (sp3d5s\* representation including spin-orbit interaction) with interorbital coupling limited to nearest neighbors.

The n- and p-layers are highly doped to provide electrons/holes to the MQW, and the MQW forms quantum-mechanical density of states (DOS) serving as recombination centers for electrons and holes. The n/p layers and the QWs contain high carrier density, typically on the order of  $10^{12}\,\mathrm{cm}^{-2}$ . In those regions, carrier scattering is strong. Since they are separated by large tunneling barriers, we consider each of them as a local equilibrium carrier reservoir with a unique local quasi Fermi level ('equilibrium' or 'eq' region, marked green in Figure 1). Individual reservoirs are connected to one another via tunneling and thermionic emission. The tunneling barriers are treated as non-equilibrium (or 'neq', marked red in Figure 1) regions where coherent quantum transport is solved with the NEGF method.

In each reservoir, an imaginary optical potential ( $\eta$ ) is included in the diagonal of the Hamiltonian<sup>[15]</sup> to mimic the sum of all scattering mechanisms. The effect of  $\eta$  leads to broadened states in the quantum wells, and the value of  $\eta$  is directly related to the scattering rate.<sup>[16]</sup> A more rigorous calculation of each scattering mechanism would be numerically unfeasible – given high material disorder and high carrier density in the LED (thus

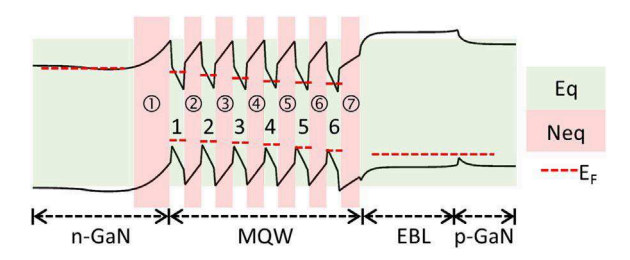


**Figure 1.** LED structure that consists of an n-GaN layer; a low-doped active region made of InGaN/GaN MQW; an AlGaN electron-blocking layer and a p-GaN layer. The equilibrium (eq — green) and non-equilibrium (neq-red) regions are marked in different colors. Each eqregion has a unique quasi Fermi level, for holes and electrons as indicated by a red dashed line. The Fermi level drops across the device are depicted not to scale to emphasize that they are different from one QW to the next. The actual Fermi level drop across the 6 QWs at normal operation of 2.9 V is only 25 meV for electrons and 176 meV for holes.

strong scattering). Instead a constant  $\eta$  of 100 meV was used in the equilibrium regions, which matches experimental measurement of optical linewidth and is numerically very efficient. For comparison and only when indicated explicitly, an artificially small broadening of 10 meV is assumed as well.  $\eta$  assumes a constant, energy independent value for energies above the bandedge, and decays exponentially into the bandgap with a decay length of 50 meV. <sup>[18]</sup> This exponential decay properly accounts for transport through the band tail states. <sup>[19]</sup>

The retarded Green's function of the device is solved by recursively inverting

$$G_{\text{Device}}^{R} = \left[ E - H_{\text{Device}} - \Sigma_{\text{S}}^{R} - \Sigma_{\text{D}}^{R} - \eta \right]^{-1} \tag{2}$$

following the partitioning in Figure 1. Note that the device Hamiltonian, Green's functions, and self-energies shown in the above equation and in the rest of this paper are matrices with respect to the tight binding orbital parameter and atomic layer index and depend on the energy and in-plane momentum as parameters. In-plane periodicity of the Hamiltonian matrices is incorporated with the Bloch theorem. The lesser Green's function is solved for each individual sub-region (eq or neq). For the 'i-th'equilibrium region (eq) with a local Fermi level  $\mu_i$ , its lesser Green's function is solved with:

$$G_{i,eq.}^{<} = -f(\mu_i)(G_i^R - G_i^{R\dagger})$$
(3)

For the 'j-th' non-equilibrium region (neq), the lesser Green's function is solved with:

$$G_{j,noneq.}^{<} = G_{j}^{R} \Sigma_{j}^{<} G_{j}^{R\dagger} \tag{4}$$

Here  $G_j^R$  is the submatrix of  $G_{\text{Device}}^R$  in the region j, and  $\Sigma_j^<$  is the sum of the contact self-energy of region j due to its coupling with the neighboring equilibrium regions j-1 and j + 1

$$\Sigma_{i}^{<} = -f(\mu_{i+1})(\Sigma_{i+1}^{R} - \Sigma_{i+1}^{R\dagger}) - f(\mu_{i-1})(\Sigma_{i-1}^{R} - \Sigma_{i-1}^{R\dagger})$$
 (5)

Here, f denotes the occupancy function, which for electron is the Fermi distribution function. The left and right connected self-energies  $\Sigma_{j+1}^R$ ,  $\Sigma_{j-1}^R$  appear in the standard recursive Green's function algorithm and describe the coupling of region j with its neighboring regions (see Ref. [5]). Note that in this way, all quantum wave effects of surrounding regions are included in the solution of the j-th region. [15]

The charge density in each region (eq and neq) 'i' is solved as

$$n_i = \frac{-2i}{A} \sum_{\mathbf{k}} \int \frac{dE}{2\pi} tr \left\{ G_i^{<}(\mathbf{k}, E) \right\}$$
 (6)

Coherent current density is only solved in the neq regions

$$J_{j} = \frac{-2e}{\hbar A} \sum_{k} \int \frac{dE}{2\pi} tr \left\{ (\Sigma_{j-1}^{R} - \Sigma_{j-1}^{R\dagger}) G_{j}^{R} (\Sigma_{j+1}^{R} - \Sigma_{j+1}^{R\dagger}) G_{j}^{R\dagger} \right\}$$

$$\left( f_{j-1} - f_{j+1} \right)$$
(7)

Note that quantities in Eqs. (5) through (7) are written for electrons. A is the normalization area in the cross-section;  $tr\{...\}$ 



denotes trace over orbitals;  $\Sigma_{\mathbf{k}}$  denotes summation over in-plane momentum. The same equations can be applied to holes by replacing the electron occupancy function f with the hole occupancy

replacing the electron occupancy function f with the hole occupancy function 1-f, and using the hole Fermi levels for each eq region. Electrons and holes are solved simultaneously for each sub-region in the device.

Total current must be conserved throughout the device, therefore, electron and hole Fermi levels must be solved iteratively until the net current density, that is the sum of inflow, outflow and recombination current density is zero

$$J_{i-1}^{e/h} - J_i^{e/h} \mp J_i^R = 0 \tag{8}$$

Here  $J_j^{e/h}$  is the coherent current density flowing out of QW j, calculated with Eq. (7) and superscript 'e/h' denotes 'electron' or 'hole' current.  $J_j^R$  is the total recombination current, which is the sum of Shockley–Read–Hall (SRH), radiative, and Auger components

$$J_i^R = J_i^{SRH} + J_i^{RAD} + J_i^{AUG} \tag{9}$$

The recombination current in each quantum well is calculated from its equilibrium density via the well-established 'ABC' equations, [20] using equilibrium charge density calculated from Eq. (6). Parameters  $A=2.9\times10^6\,\mathrm{s^{-1}}$ ,  $B=1.48\times10^{-11}\,\mathrm{cm^3s^{-1}}$ , and  $C=1.6\times10^{-30}\,\mathrm{cm^6s^{-1}}$  used in this work are extracted from experimental benchmark data.

The coherent current, recombination current in QW i are functions of Fermi levels in QWs i-1, i, i+1. Therefore, solving for current conservation is equivalent to solving a system of non-linear equations:

$$\Delta J_i^{e/h} \Big( \mu_{i-1}^{e/h}, \mu_i^{e/h}, \mu_{i+1}^{e/h} \Big) = 0, (i = 1 \dots N)$$
 (10)

 $\mu_i$  denotes the Fermi level in QW i, and N is the total number of QWs.  $\mu_0$  and  $\mu_{N+1}$  correspond to the source/drain Fermi levels respectively. After the total current is conserved, physical quantities including charge and current densities are solved once again with the converged Fermi levels, and individual region's charge densities are concatenated in space to form a charge density profile of the total device.

The electrostatic potential is calculated self-consistently by solving the Poisson equation with the quantum charge density. The ionized doping concentration is calculated with the incomplete ionization model, using 0.16 eV ionization energy for Mg.[21] Piezoelectric polarization is calculated analytically from strain tensors, with parameters including elastic constants, piezoelectric constants and spontaneous polarization taken from Ref. [22] assuming linear alloy scaling. The tight-binding parameters are fitted<sup>[23]</sup> against bulk DFT calculations using VASP with the HSE06 potentials. The growth direction is the c-plane and the Wurtzite crystal structure is explicitly represented in this atomistic basis. The energy and momentum meshes for the quantum transport simulation are obtained with an adaptive-refinement method that optimizes around the peaks of charge density and current in each region.[24]

## 3. Results

The model is applied to simulate a commercial LED device. Figure 1 shows the conduction and valance band diagram of the LED active region, which consists of (from left to right): 15.5 nm n-GaN layer doped at  $1\times10^{18}\,\mathrm{cm^{-3}}$ , 20.7 nm n-type GaN layer doped at  $4\times10^{18}\,\mathrm{cm^{-3}}$ , 6 repeating  $\mathrm{In_{0.13}Ga_{0.87}N/GaN}$  (3.1 nm/4.6 nm) QWs unintentionally n-doped at  $2\times10^{15}\,\mathrm{cm^{-3}}$  and a 24.8 nm  $\mathrm{Al_{0.12}Ga_{0.87}N}$  electron-blocking layer followed by a 15.5 nm GaN layer, both p-doped at  $4\times10^{19}\,\mathrm{cm^{-3}}$ .

The colormap in **Figure 2** shows the position and energy distributed charge densities calculated from Eq. (6) with k=0. Setting k=0 enables visualization of the spatial and energetic distribution of the quantum states without loss of generality. Also shown in Figure 2 are the contour lines of density of states (DOS), which map out the available states for electrons to fill in. The bulk-based conduction and valence band edges are also included in the plot as a guide to the eye. Given typical InGaN LED barrier widths are in the range of a few nanometers, the

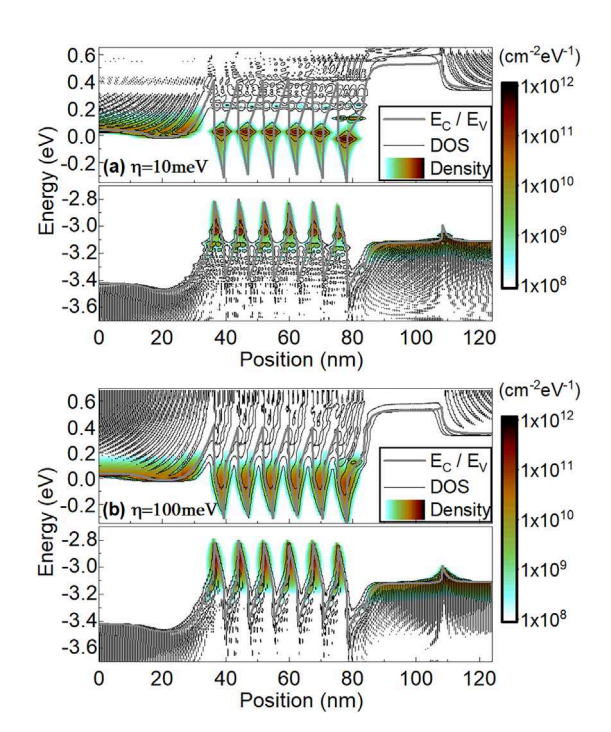


Figure 2. Energy-resolved electron, hole density of states (contour lines) filled with electrons and holes (color contours). The bulk-based conduction and valence band edges serve as a guide to the eye and only enter the calculation in the definition of the empirical scattering strength  $\eta$ . States in the QW are broadened due to  $\eta$  and coupled to each other. (a)  $\eta=10\text{meV}$  is a typical broadening in GaAs and InP based devices. The quantum well states are broadened but still distinct. (b)  $\eta=100\,\text{meV}$  is a broadening that corresponds to experimental optical linewidth measurements. The various hole states are all cross coupled and also the electron states broaden energetically to about half the height of the quantum wells. These broadened states serve as injectors and receptors for tunneling across the barriers.  $\eta=100\,\text{meV}$  leads to the quantitative agreement with experimental data shown below and is used in all other simulations presented here. (Similar figure containing preliminary data can be found in Ref. [13])

states in the QWs are broadened and coupled to each other. Carriers are distributed in energy across these broadened states.

A distinct quantum interference pattern is observed throughout the energy range of interest, and as a result, no distinction should be made between 'classical' and 'quantum' regions. Coupling between continuum and discrete states occurs naturally. The broadening of states is a direct manifestation of finite carrier lifetime, due to frequent scattering events and coupling to the open leads. Stronger scattering, mimicked by a higher value of  $\eta$ , leads to larger state broadening and more cross-coupling between various states, as shown by comparison of Figure 2(a) and (b). Therefore, carrier transport occurs through a complex, extended structure, and is directly influenced by the overall quantum-mechanical properties of the system. The electrons fill all the QW ground states and partially fill the excited states. The hole states are spaced much more closely in energy due to their larger effective mass. The heavy and light hole bands are explicitly coupled in this model due to breaking of translational symmetry. The hole charge density spreads in energy over multiple confined quantum states.

The local band edges are also shown in Figure 2. Alloy values are interpolated from the bulk constituents. [22] In a semiclassical model, carrier transport is strictly limited by the energy position of the band edges, allowing transport to only occur above Ec and below Ev. However, at this nanoscale new quantum states emerge that render local bulk band edges almost irrelevant.

Figure 3 plots the position-resolved electron and hole density (integrated over all energy and momentum) throughout the device. Band profile and local Fermi levels are plotted as well. For electrons, the Fermi level drop is very small (25 meV) across the sequence of 6 QWs: the electrons are well transported across the active region. In contrast the total Fermi level drop for the holes is 176 meV. Clearly the holes are not well transported and large Fermi level drops are needed to support required total current conservation. As a result, electron density is well spread throughout the device, while the hole density distribution is heavily skewed towards the p-side QWs.

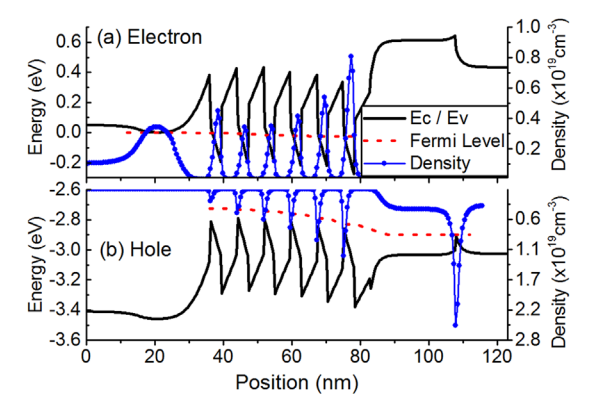


Figure 3. (a) Conduction band profile with electron density and (b) valence band profile with hole density at 2.9 V bias. Note that local Fermi levels (red dashed lines) are only defined in the leads and QWs, where those regions are considered in a local thermal equilibrium. The continued lines across barriers are meant to guide the eye. The Fermi level drops across the device is 25 meV for electrons and 176 meV for holes. (Similar figure containing preliminary data can be found in Ref. [14])

**Figure 4**(a) compares the *I–V* characteristics between simulated results and experimental data. Preliminary I-V data were also published and discussed in Ref. [13,14]. The experimental structure contains series resistance in the order of a few m $\Omega \cdot \text{cm}^2$ , mainly induced by the contacts and spreading layer. The simulations presented here use a fitted series resistance of  $2.0 \,\mathrm{m}\Omega \cdot \mathrm{cm}^2$ . A well-known challenge of traditional semiclassical-based model is the difficulty in obtaining a good *I–V* match with experiment. Typically, a much larger bias voltage is needed to model the same current as measured in experiments. Methods such as including large alloy fluctuation in the simulation<sup>[25]</sup> have been proposed as remedies. However, the unrealistic turn-on voltage under normal conditions is an indication of missing critical transport physics in semiclassical models. Therefore, a key achievement here is that the turn-on voltage of this complex device is modeled correctly with our approach.

LEDs typically operate under a variety of temperatures, and a realistic operating condition<sup>[26]</sup> for LEDs is around 85 °C. Figure 4 (b) presents the *I*–*V* characteristics in a temperature sensitivity study in the range 320–400 K. As the carrier temperature inside the LED increases, the *I–V* curves shifts to a lower voltage. Higher temperatures lead to broadened energy-distribution of carriers in the quantum wells, leading to higher thermionic emission at the same voltage. As a result, higher temperatures lead to earlier device turn on. The simulation result shows the LED forward voltage at 20 A cm<sup>-2</sup> varying between 2.75–2.92 V under a realistic temperature variation of 80 K. An assumed electron temperature of 360 K results in the best match with our experimental data, which in turn agrees reasonably well with experimental evidence. [26] Note that the temperature variation is captured in the model through the Fermi distribution (Eqs. 3-7) only. Nonequilibrium carrier distributions are not included. However, recent work has shown that there is a vanishing probability for long range carrier tunneling. [27] Thus, neither electrons nor holes can propagate far enough without energy loss to cause significant hot carrier formation.

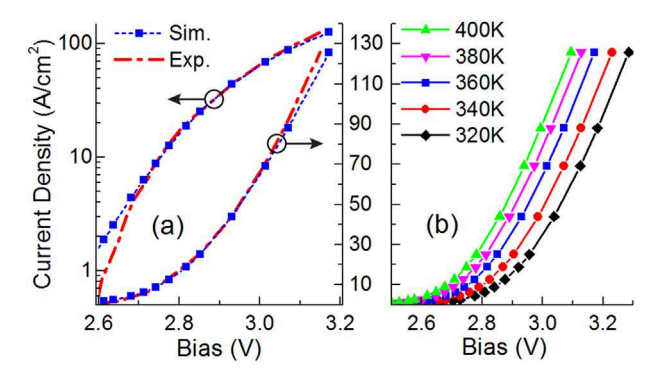
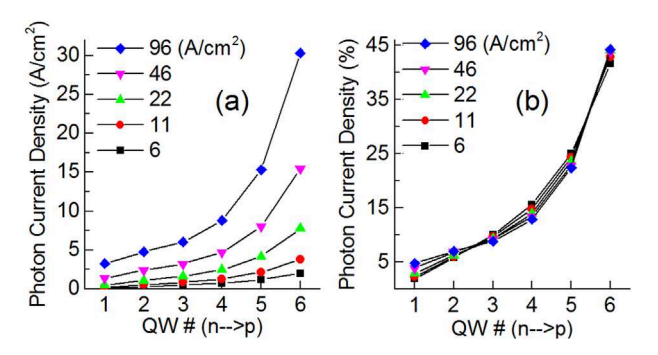


Figure 4. (a) I-V comparison with experiment shows good quantitative match on a linear and a log scale. A 2.0 m $\Omega$  · cm2 series resistance, 360 K electron temperature, and 100 meV spectral broadening in the quantum wells are assumed in the simulation. (b) I-V Simulations for various temperatures ranging from 320 to 400 K result in a variation of  $\approx$  170 meV in turn-on voltage.



**Figure 5.** Photon current density profile for each quantum well with the total current density as a parameter. (a) absolute photo emission current, (b) relative photon emission current. QWs closer to the p-side emit more light, which matches experimental observation.

**Figure 5** shows the photon emission current density from each quantum well at different drive currents. The main observation is that light emission is heavily skewed towards the p-side, with the right most QW emitting about 40% of the total light. The distribution becomes more uneven with increasing drive current. This is in good general agreement with previous experiments, [28,29] although the experimentally observed emission profile is even more skewed towards the last two QWs. Such a phenomenon is an indication of non-uniform carrier distribution among QWs at normal operation conditions, and has a negative impact on the LED's quantum efficiency.

**Figure 6** plots the percentage of the radiative recombination versus different drive current (square markers). This ratio is equivalent to the internal quantum efficiency (IQE). The simulation data predicts a droop roll-over at around  $6\,\mathrm{A\,cm^{-2}}$ . The relative importance of leakage (overflow of carriers out of the entire active region) vs. Auger to efficiency droop has historically been a debating point. Conclusions from traditional modeling methods tend to vary depending on simulation condition and choice of parameters. [30] A recent experiment identifies Auger recombination as the main mechanism responsible for the efficiency droop in InGaN/GaN LEDs. [31]

Our modeling results indicate direct (non-Auger-assisted) leakage current to be negligible, as its contribution to the total current is well below 1%. The efficiency droop is numerically captured in the model (Figure 6) and solely attributed to Auger recombination. This is a natural outcome of the model's assumptions, since the 'ABC' model was applied to treat recombination.

Figure 7 shows the energy-resolved current density at zero inplane momentum ( $J(E,\vec{k}=0)$ ) in Eq. (7)). Results for a single barrier (barrier #3 in Figure 1) in the MQW ((a) and (d)) and the two end barriers ((b) EBL for electrons and (c) n-GaN layer for holes) are plotted. All other barriers' current density exhibits very similar characteristics with barrier #3 and are therefore omitted. Two different scattering rates ( $\eta=10$  and 100 meV) are plotted together for comparison. At  $\eta=10$  meV, corresponding to the lower scattering rate, the current density exhibits distinct (and broadened) resonances, and the current contribution from various confined states can be identified. At  $\eta=100$  meV, which corresponds to the realistic scattering rate, the various states

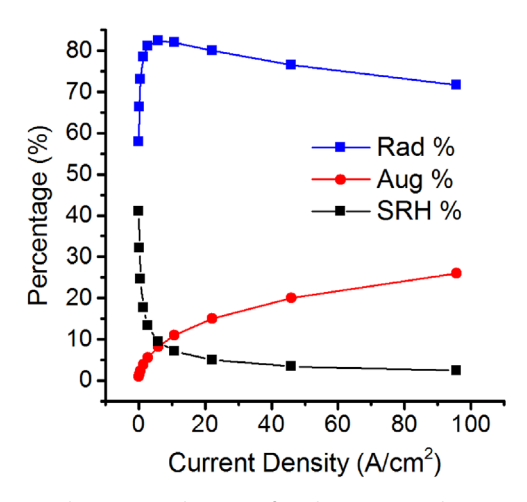


**Figure 6.** Relative contribution of radiative recombination, Auger recombination, and SRH to the total current density.

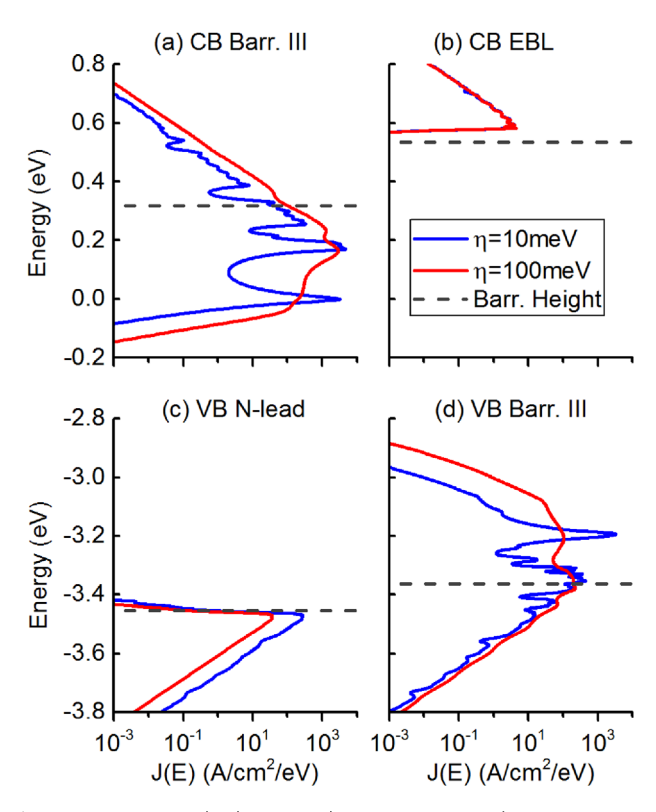


**Figure 7.** Energy-resolved current density at zero in-plane momentum  $J\left(E,\vec{k}=0\right)$  for (a) middle barrier (#3) in the conduction band (b) EBL in the conduction band (c) n-GaN layer in the valance band (d) middle barrier (#3) in the valance band (indexing follows **Figure 1**).  $\eta=10$  versus 100 meV are plotted together for comparison. Barrier heights are marked with dashed lines in each figure. (a), (d) represents typical transport scenario in MQW LED where the majority of transport occurs under the barrier via tunnelling; (b), (c) represents electron and hole leakage current out of the active region. (Similar figures containing preliminary data can be found in Ref. [14]).



become cross-coupled and the current density curves become smooth.

What is noteworthy here is that in the active region, the majority of current contribution comes from tunneling under the barriers, as seen in Figure 7(a) and (d). The respective barrier height is marked with a dashed line in each figure. It shows that the major part of current lies below the barrier both in the conduction band and in the valance band. After taking into account all relevant in-plane momenta and integrating over the relevant energy ranges, almost all the electron current (99%) and majority of hole current (75%) are tunneling current densities.

Comparing 4(a) vs. (b), it becomes clear that the electron current density flowing through the EBL is much less compared to the transport current through MQW barriers. The same conclusion holds for holes (by comparing (d) and (c)). The end barriers seen by electrons (EBL) and holes (n-GaN) are too large (height >10kT above Fermi level, thickness >20 nm) for direct leakage to play any noticeable role. Therefore, only Auger recombination can cause the majority of IQE droop.

#### 4. Conclusion

A numerically efficient, multi-scale multi-physics NEGF model is introduced and applied to model a realistically extended commercial LED device. The model produces quantitative agreement with experimental I-V characteristics. The carrier temperature is identified to be around 85 °C, and light emission is most prominent at the QW closest to the p-side. Efficiency droop is observed in the numerical data and attributed to strong contribution from Auger recombination, since direct leakage out of the active region is found to be negligible compared to Auger recombination. Majority of electron and hole conduction in the MQW region occurs through tunneling below the barriers. Physical insights into local quasi Fermi level drops, state-to-state coupling and broadening, relative importance of leakage and Auger currents, and dominance of optical recombination of specific QWs open up opportunities for coming LED design optimizations.

# **Acknowledgements**

We acknowledge helpful discussions with Daniel Mejia and Xinchen Guo. This research was supported in part by Lumileds as well as the Intel Parallel Computing Center (IPCC). The use of nanoHUB.org computational resources operated by the Network for Computational Nanotechnology funded by the US National Science Foundation under Grant Nos. EEC-0228390, EEC-1227110, EEC-0228390, EEC-0634750, OCI-0438246, OCI-0832623, and OCI-0721680, as well as the use of Blue Waters (part of National Science Foundation ACI 1238993) is gratefully acknowledged. The model has been implemented in NEMO5 (see Ref. [32]) and is available on nanoHUB within academic open source license.[33]

# **Conflict of Interest**

The authors declare no conflict of interest.

## **Keywords**

light-emitting diodes, modeling, multi-scale multi-physics, NEGF (nonequilibrium Green's function), nitride

> Received: August 28, 2017 Revised: November 10, 2017 Published online: December 27, 2017

- [1] Y. C. Shen, G. O. Mueller, S. Watanabe, N. F. Gardner, A. Munkholm, M. R. Krames, Appl. Phys. Lett. 2007, 91, 141101.
- C. Weisbuch, M. Piccardo, L. Martinelli, J. Iveland, J. Peretti, J. S. Speck, Phys. Status Solidi A 2015, 212, 899.
- [3] M. H. Crawford, IEEE J. Sel. Top. Quantum Electron. 2009, 15, 1028.
- [4] M. Goano, F. Bertazzi, X. Zhou, M. Mandurrino, S. Dominici, M. Vallone, G. Ghione, A. Tibaldi, M. Calciati, P. Debernardi, F. Dolcini, F. Rossi, G. Verzellesi, M. Meneghini, N. Trivellin, C. D. Santi, E. Zanoni, E. Bellotti, Proc. SPIE 9742, Physics and Simulation of Optoelectronic Devices XXIV, 974202, 2016.
- [5] R. Lake, G. Klimeck, R. Bowen, D. Jovanovic, J. of Appl. Phys. 1997, 81,
- [6] T. Kubis, C. Yeh, P. Vogl, A. Benz, G. Fasching, C. Deutsch, Phys. Rev. B 2009, 79, 195323.
- [7] M. Luisier, G. Klimeck, Phys. Rev. B 2009, 80, 155430.
- C. Bowen, G. Klimeck, R. Lake, W. R. Frensley, T. Moise, J. Appl. Phys. 1997, 81, 3207.
- G. Klimeck, R. Lake, D. Blanks, C. L. Fernando, C. Bowen, T. Moise, Y. C. Kao, Phys. Status Sol. B, Basic Res. 1997, 204, 408.
- [10] S. Steiger, R. G. Veprek, B. Witzigmann, Proc. 13th Int. Workshop Comput. Electron. pp. 1-4 (2009).
- [11] A. Shedbalkar, Z. Andreev, B. Witzigmann, Phys. Status Solidi B 2016, 253, 158.
- [12] M. Auf der Maur, B. Galler, J. Comput. Electron. 2015, 14, 398.
- [13] J. Geng, P. Sarangapani, E. Nelson, C. Wordelman, B. Browne, T. Kubis, G. Klimeck, Proc. NUSOD 2016, IEEE, pp. 107-108, 2016.
- [14] J. Geng, P. Sarangapani, E. Nelson, C. Wordelman, B. Browne, T. Kubis, G. Klimeck, Proc. SPIE 2017, 10098, 1009813.
- [15] G. Klimeck, R. Lake, R. C. Bowen, W. R. Frensley, T. Moise, Appl. Phys. Lett. 1995, 67, 2539.
- A. Wacker, Phys. Rep. 2002, 357, 1.
- [17] K. P. O'Donnell, T. Breitkopf, H. Kalt, W. Van der Stricht, I. Moerman, P. Demeester, P. G. Middleton, Appl. Phys. Lett. 1997, 70, 1843.
- [18] O. Ambacher, D. Brunner, R. Dimitrov, M. Stutzmann, A. Sohmer, F. Scholz, Jpn. J. Appl. Phys. 1998, 37, 745.
- [19] M. A. Khayer, R. K. Lake, J. Appl. Phys. 2011, 110, 074508.
- [20] J. Piprek, Phys. Status Solidi A 2010, 207, 2217.
- [21] M. E. Levinshtein, S. L. Rumyantsev, M. S. Shur, Properties of Advanced Semiconductor Materials: GaN, AlN, InN, BN, SiC, SiGe, Wiley, New York 2001.
- [22] F. Bernardini, in Nitride Semiconductor Devices: Principles and Simulation, J. Piprek (Ed.), Wiley-VCH, Weinheim 2007, pp. 49.
- [23] Y. Tan, M. Povolotskyi, T. Kubis, T. B. Boykin, G. Klimeck, Phys. Rev. B **2016**, 94, 045311.
- G. Klimeck, R. K. Lake, R. Ch. Bowen, Ch. L. Fernando, W. R. Frensley, VLSI Design 1998, 6, 107.
- [25] T. J. Yang, R. Shivaraman, J. S. Speck, Y. R. Wu, J. Appl. Phys. 2014, 116, 113104.
- [26] C. A. Hurni, A. David, M. J. Cich, R. I. Aldaz, B. Ellis, K. Huang, A. Tyagi, R. A. DeLille, M. D. Craven, F. M. Steranka, M. R. Krames, Appl. Phys. Lett. 2015, 106, 031101.
- [27] J. Geng, K. Wang, P. Sarangapani, E. Nelson, C. Wordelman, B. Browne, T. Kubis, G. Klimeck, Proc. Int. Workshop Comput. Nanotech. pp. 1-4 (2017).





- [28] Y. C. Shen, J. J. Wierer, M. R. Krames, M. J. Ludowise, M. S. Misra, F. Ahmed, A. Y. Kim, G. O. Mueller, J. C. Bhat, S. A. Stockman, P. S. Martin, Appl. Phys. Lett. 2003, 82, 2221.
- [29] A. David, M. J. Grundmann, J. F. Kaeding, N. F. Gardner, T. G. Mihopoulos, M. R. Krames, Appl. Phys. Lett. 2008, 92, 053502.
- [30] J. Piprek, Appl. Phys. Lett. 2015, 107, 031101.

- [31] J. Iveland, L. Martinelli, J. Peretti, J. S. Speck, C. Weisbuch, Phys. Rev. Lett. 2013, 110, 177406.
- [32] J. E. Fonseca, T. Kubis, M. Povolotskyi, B. Novakovic, A. Ajoy, G. Hegde, H. Ilatikhameneh, Z. Jiang, P. Sengupta, Y. Tan, G. Klimeck, J. Comput. Electron. 2013, 12, 592.
- [33] See https://nanohub.org/groups/nemo5distribution for more information about access to NEMO5 resources; accessed 13 September 2017.